1 # Sequestration of antimony on calcite observed by

2 # time-resolved nanoscale imaging

3 *François Renard[1,2], Christine V. Putnis[3,4], German Montes-Hernandez[2], Helen E. King[5], Gijs D.*

4 *Breedveld[1,6], Gudny Okkenhaug[6,7]*

5 [1]Department of Geosciences, Physics of Geological Processes, University of Oslo, Norway

6 [2]Univ. Grenoble Alpes, CNRS, ISTerre, 38000, Grenoble, France

7 [3]Institut für Mineralogie, University of Münster, Corrensstrasse 24, 48149 Münster, Germany

8 [4]The Institute for Geoscience Research (TIGeR), Department of Chemistry, Curtin University,

9 Perth, 6845, Australia

10 [5]Department of Earth Sciences, Utrecht University Budapestlaan 4, 3584 CD Utrecht, The

11 Netherlands

12 [6]Norwegian Geotechnical Institute, box 3930, Ullevål Stadion, 0806 Oslo, Norway.

13 [7]Norwegian University of Life Sciences, Faculty of Environmental Sciences and Natural

14 Resource Management, box 5003, 1432 Ås, Norway

15

17 ABSTRACT. Antimony, which has damaging effects on the human body and the ecosystem, can

18 be released into soils, ground- and surface waters either from ore minerals that weather in near

19 surface environments, or due to anthropogenic releases from waste rich in antimony, a

20 component used in batteries, electronics, ammunitions, plastics and many other industrial

21 applications. Here, we show that dissolved Sb can interact with calcite, a widespread carbonate

22 mineral, through a coupled dissolution-precipitation mechanism. The process is imaged in-situ,

23 at room temperature, at the nanometer scale by using an atomic force microscope equipped with

24 a flow-through cell. Time-resolved imaging allowed following the coupled process of calcite

25 dissolution, nucleation of precipitates at the calcite surface and growth of these precipitates.

26 Sb(V) forms a precipitate, whereas Sb(III) needs to be oxidized to Sb(V) before being

27 incorporated in the new phase. Scanning-electron microscopy and Raman spectroscopy allowed

28 identification of the precipitates as two different calcium-antimony phases ($Ca_2Sb_2O_7$). This

29 coupled dissolution-precipitation process that occurs in a boundary layer at the calcite surface

30 can sequester Sb as a solid phase on calcite, which has environmental implications as it may

31 reduce the mobility of this hazardous compound in soils and groundwaters.

32
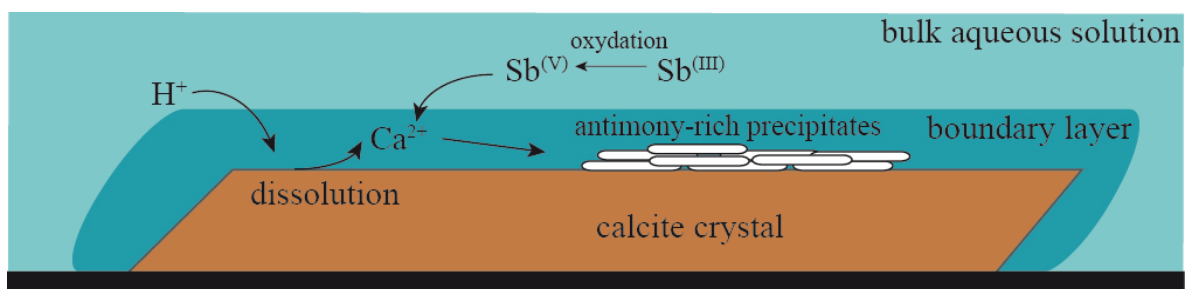
Introduction

34   The environmental presence and behavior of antimony (Sb), a hazardous substance as a solid

35   or in solution, is gathering increased attention due to its increasingly extensive use in various

36   products and its fate in the environment. The use of Sb includes applications as flame retardant

37   in plastics, rubbers, textiles, brake pads, pigments, paints, ceramics, and semiconductor materials

38   such as GaSb and InSb in electronic devices. In addition, it is present as a lead alloy in storage

39   batteries and ammunitions. Substantial Sb emissions are related to mining and smelting activities

40   and spent ammunitions at shooting ranges[1,2]. Its widespread use results in high concentrations

41   present in waste, including air pollution control residues (i.e., ashes of flue gas treatment) from

42   waste incineration[3]. Consequently, soils can show significant concentrations of Sb[4,5], leading to

43   elevated levels in soil pore water and groundwater[5].

44   Antimony can be found in four oxidation states (-III, 0, III, and V), of which Sb(III) as neutral

45   antimonite ($Sb(OH)_3$) and Sb(V) as antimonate ($Sb(OH)_6^-$) oxyanion are the most common

46   species in natural environments[6]. In oceans, the concentration of dissolved antimony is around

47   0.2 $\mu g\ L^{-1}$. In non-polluted freshwater[7] it is usually below 0.2 $\mu g\ L^{-1}$ but can sometimes reach 5

48    $\mu g\ L^{-1}$, while the average concentration in world rivers[6,8] is close to 1 $\mu g\ L^{-1}$. Comparatively high

49   concentrations of up to 95 $\mu g\ L^{-1}$ antimony have been recorded in polluted groundwater and

50   soils, where the antimony source was either natural, such as volcanic glass[9], or anthropogenic

51   e.g., contaminated soil and other industrial wastes[6]. Groundwater flowing out of an abandoned

52   antimony mine near Goesdorf, Luxemburg[8] was found to contain Sb at a concentration of up to

53   2.2 mg L^{-1} at pH 7-8. The concentration in alkaline groundwater (pH~8) near an active mine in

54   the Hunan province in China[10] was found to reach 11.4 mg L^{-1}; and all dissolved antimony was

55   in the form of Sb(V). Laboratory leaching of similar mining impacted soils[1] showed water

56   extractable concentrations of up to 748 mg kg^{-1} of soils and concentrations in water of up to 103

57   mg L^{-1} after 7 days contact time, for a pH range between 5 and 7.

58   In calcium (Ca) rich environments as calcareous soils and alkaline waste materials, Ca is

59   suggested as an important sink for Sb. Calcium antimonates ($Ca[Sb(OH)_6]_2$ and $Ca_{1+x}Sb_2O_6OH_{2-2x}$

60   ) belong to the family of roméite minerals[11]. The solubility of roméite at room temperature[12]

61   and pH 8 is of the order of 4 mg L^{-1}. The solubility product of romeite varies as this mineral may

62   contain vacancies and crystallographic defects that affect dissolution[13]. Solubility between $10^{-3.4}$

63   and $10^{-4.8}$ mol L^{-1} at 25°C has been proposed, with a factor 60 difference between extreme

64   values[13]. In several industrial waste systems, the solubility product of a hydrated calcium

65   antimonate indicates this mineral should precipitate[14]. Based on XANES spectroscopy and

66   equilibrium calculations, it has been proposed that this mineral controls the solubility of

67   antimony in soils near active antimony mines in China[1] or during the leaching of bottom ash

68   from incinerated municipal waste[14]. However, to our knowledge, no direct evidence of the

69   presence of roméite or another calcium antimony phase was provided in these studies, such as

70   Raman spectroscopy or X-ray diffraction identification.

71   The dissolution-precipitation reaction of roméite at calcite interfaces could contribute to long-

72   term spatial and temporal storage of antimony in carbonate-rich environments. The main

73   objectives of the present study are to 1) characterize the coupling between calcite dissolution and

74   precipitation of Ca - Sb phase(s); 2) quantify the spatial and temporal evolution of the precipitate

75   nuclei; 3) hypothesize if a coupled dissolution-precipitation process could immobilize Sb at the

76   calcite surface.

Materials and methods

A calcite crystal (Iceland spar, Vizcaya, Mexico) was obtained from the Natural History

Museum in London. ICP-OES (inductively coupled plasma - optical emission spectroscopy)

analyses indicate the high purity of the calcite crystal, with trace amounts of Mn (31 ppb), Mg

(2.8 ppb) and Sr (11.4 ppb). Fresh calcite fragments (ca. 3 x 2 x 1 mm) were prepared directly

before each experiment by cleaving the calcite crystal parallel to the {10-14} plane.

The calcite surfaces were scanned in a room with controlled temperature (22±1 °C) and

humidity (40%) using a Bruker Multimode Atomic Force Microscope (AFM) operating in

contact mode (Supporting Information). At the beginning of each experiment, deionized water

was injected over the calcite surface for several minutes, to observe any reaction or dissolution.

Then, antimony-free solutions and solutions with a controlled amount of Sb (Sb(III) or Sb(V)),

with the same constant ionic strength (0.05 M) and various controlled pH values between 2 and

8, were injected (Table S1). Several solutions with identical compositions were used to test the

reproducibility of the obtained results.

The same procedure described below was followed in each experiment to ensure results could

be compared between experiments. Firstly, deionized water was injected for 10 minutes and 5

images were acquired. Secondly, a solution without Sb and at the desired constant pH was

injected for another 10 minutes and 5 images were acquired. Thirdly, solutions with increasing

Sb concentrations were injected, with 5 images acquired at 1.5 minute intervals, then the AFM

tip was lifted for 10 minutes after which another image was acquired, then the AFM tip was

lifted for 1 hour and a further series of AFM images were acquired. Following this procedure,

calcite dissolution was followed in the AFM for several hours. As a consequence, the injection

99   was intermittent, with an average flow rate of 22 $\mu L \cdot s^{-1}$ and residence time between 1.5 minute

100   and several hours (Supplementary Information).Then the sample was removed from the flow-

101   through cell, left in contact with the solution for 12 to 20 hours to allow sufficient time for

102   reaction, and then imaged again. The same samples were used for scanning electron microscopy

103   imaging and Raman spectroscopy characterization (Supporting Information).

104   **Results**

105   *Dissolution at calcite surface:* The cleaved calcite {10-14} surface is characterized by the

106   presence of steps (Figure S1a). Direct in situ observations showed that in contact with water and

107   aqueous solutions the calcite surface dissolves along steps that retreat, as well as through the

108   formation of etch pits with typical rhombohedral shapes (Figure S1b). Etch pit steps were

109   typically one unit cell (3.1 Å) high, before deepening. These pits spread sideways to merge and

110   remove successive unit-cell heights layer by layer. The average spreading rate $v_{avg}=(v_+ + v_-)/2$

111   was measured from etch pits spreading between two successive AFM scans. Here, v_+ and v_- are

112   the velocities of the obtuse and acute steps of etch pits, respectively[15]. At pH below 4, the

113   dissolution was so fast that it was not possible to measure etch pit spreading rates. At pH

114   between 4.5 and 8, spreading rates and their standard deviation could be calculated from multiple

115   measurements and found to fall in the range $v_{avg} = 2.6\pm1.3$ to 4.1 ± 0.5 $nm \cdot s^{-1}$, a range of values

116   previously reported for calcite[15]. No clear effect of Sb on the overall etch pit spreading rate could

117   be observed. However, in all experiments where Sb(V) was injected, the shape of the initial

118   rhombohedral etch pits evolved within minutes to show a rounding curve at the obtuse corner

119   that seemed to be pinned (Figure S1c, d).

120   *Formation of precipitates*: The precipitates initially formed as small "spots", with an average

121   height of a few nanometers, just within the limits of AFM recognition under the given fluid

122   conditions and contact mode. They were distributed at kink sites on the calcite surface (Figure 1)

123   and showed low adhesion, as they were easily moved by the scanning AFM tip at the initial stage

124   of precipitation. With time, they tended to localize near step edges (Figure 1) or near deep etch

125   pits (Figure 2b) or, close to locations where dissolution was more intense. This means that

126   dissolution sites where more calcium was released control the nucleation process of the

127   precipitates. Initially the precipitates nucleated as individual particles with a rounded shape

128   (Figure S2a). Then these particles either piled up or aggregated to form larger particle clusters

129   (Figure S2 b-d). They grew in size into larger rounded structured aggregates until they covered

130   the whole calcite surface (Figure 2a). Even at this stage, they were weakly attached to the

131   surface, as successive scans on the same area showed that fewer particles were present than in

132   the surroundings (Figure 2a), which we interpret by the displacement of particles by the scanning

133   AFM tip.

134   The shape and size of these precipitates could be measured in all experiments where they were

135   observed and all showed that they formed patches with a more or less circular perimeter, a low

136   height to diameter aspect ratio (Figure S3), and no evidence of crystallographic facets at the

137   onset of precipitation. We have chosen to measure particles whose diameter is larger than 100

138   nanometers, the spatial resolution of the AFM technique used here. With time, some of these

139   particles developed facets (Figure S2d). Images were collected at different times, under different

140   conditions, and over differing areas of observation. Under all these conditions the precipitated

141   particles presented rounded perimeters. At the scale of the AFM observations tip-shaped

142   convolutions would therefore be minimal. The height and diameter of the precipitates measured

7

143   for all experiments (Figure 3) show that initially particles were quite flat (~ 10 nm), with a

144   diameter in the range 100-200 nm. These particles formed within 2 minutes after the injection of

145   Sb. With time, particles tended to grow in height, while keeping a maximum diameter smaller

146   than 800 nm and within the range 300-800 nm. During this stage, particles aggregated or merged

147   together and then grew in height to 20-120 nm. For three experiments the same particles could be

148   followed in a time sequence and their height to diameter ratio showed a positive trend with time

149   (Figure S3), demonstrating that particles first grew laterally (by the merging of smaller particles),

150   as thin discs and then grew more continuously in height. In one experiment, a linear fit of the

151   particle height with time could be performed and gives a growth rate of 0.016 nm·s^{-1} (Figure

152   S4b), whereas the diameter of the precipitates did not change significantly (Figure S4a). .With

153   time the calcite surface became covered by these particles that produced several layers of

154   precipitates (Figure 2a). These observations were seen for acidic fluids in the presence of Sb; the

155   lower the pH, the faster the calcite dissolved and more particles precipitated. Many more

156   particles nucleated and grew in the presence of Sb(V) as compared to Sb(III).

157   *Identification of the precipitates*: Evidence for dissolution of the calcite surface and

158   precipitation of a new phase was also observed in the SEM (Figure 4a) on calcite samples left 24

159   hours in the Sb solutions. In the 200 ppm Sb(V) solutions at pH 5 the calcite surface was covered

160   in precipitates along with rhombohedral etch pits seen in Figure 4b. The precipitates were

161   between 5 and 25 μm width. These particles had clear crystal facets indicating a crystalline

162   structure and showed a consistent dipyramidal form (Figure 4b). Incorporation of Sb into the

163   particles was confirmed by comparison of the EDX spectra for the particles, which showed peaks

164   for Ca Kα, Kβ and Sb Lα Lβ in the spectral region between 3 to 5 keV, and the underlying

165   calcite surface (Figure 4c). Raman spectroscopy of the precipitates produced spectra (Figure 4d)

166   with peaks listed in Table S2. The small, sharp band at 1086 cm^{-1} is consistent with the

167   symmetrical stretch of carbonate in the underlying calcite crystal[16], as are the smaller peaks at

168   156, 283 and 711 cm^{-1}. The rest of the peaks therefore originate from the precipitate itself. The

169   dominant peak in the spectrum at 624 cm^{-1} and the smaller peak at 384 cm^{-1} correspond well

170   with previously published synthetic $Ca_2Sb_2O_7$ Raman spectra[17]. This mineral was also observed

171   to form in hydrothermal experiments where calcite was left in contact with dissolved Sb[18].

172   However, the strong Raman peak documented for synthetic $Ca_2Sb_2O_7$ at 472 cm^{-1} is not present

173   in the spectra obtained from the precipitates. Similarly the published spectra do not show

174   evidence for peaks around 500 cm^{-1} that are visible in Figure 4d. This could be related to crystal

175   orientation, which is known to change the relative intensities of peaks within the Raman

176   spectra[19]. However, it may also be related to the precipitate chemistry or mixed phase as Raman

177   spectra[20] from the natural mineral oxycalcioroméite ($Ca_2Sb_2O_6O$) with a more varied

178   composition and cubic structure show dominant peaks around 500 cm^{-1}.

179   **Discussion**

180   *Dissolution-precipitation in a boundary layer*: The interactions of calcite with oxyanions, such

181   as arsenic or selenium, were reported in previous studies[21,22,23], where it was shown that etch pit

182   corners could be pinned during dissolution to result in etch pit shapes deviating from normal

183   rhombohedral etch pits, characteristic of calcite dissolving in water[15]. In the present study, a

184   similar effect was observed, demonstrating that Sb interacts with kink sites in etch pits and

185   slightly modify the dissolution process. However, this pinning does not have a measurable effect

186   on the etch pit dissolution rate that remained within the average rate for calcite in pure water (2-4

187   nm·s^{-1}).

188   During dissolution of calcite, ions are released such that the fluid-mineral boundary layer

189   becomes increasingly saturated with Ca^{2+} and CO_3^{2-} ions, this last species being protonated into

190   HCO_3^- at neutral and low pH. When the calcite surface is in contact with the Sb-bearing solution,

191   the interfacial fluid becomes supersaturated with a new Ca-Sb phase that can then precipitate. It

192   is now well-established, using real-time phase-shift interferometry and ion-specific micro-

193   electrodes, that interfacial mineral-fluids can become supersaturated with a new phase when the

194   bulk solution is undersaturated[24]. This interface-coupled dissolution-precipitation process[25,26] is

195   summarized in the graphical abstract and involves the dissolution of the calcite substrate,

196   releasing Ca^{2+}, followed simultaneously by the nucleation of precipitates, initially only less than

197   10 nanometers in diameter. The small rounded precipitate particles grew in diameter, until they

198   reached a size in the range 300-800 nm, and then grew in height to 20-120 nanometers.

199   Observations indicate that the initial particles merged with adjacent particles (Figures 3c; S2b,

200   S2d). With time the calcite surface became covered by these particles that produced several

201   layers of precipitates (Figure 2a). There is therefore a balance between nucleation of new

202   precipitates and growth of existing ones.

203   *Mechanism of dissolution precipitation*: The interface coupled dissolution-precipitation

204   reactions at the calcite surface can be schematically represented as follows:

205    $\equiv CaCO_3 + H^+ \rightarrow Ca^{2+} + HCO_3^-$ (dissolution process)

206    $Ca^{2+} + Sb^{(V)} \rightarrow Ca - Sb^{(V)}$ phase   (precipitation process)

207   The appearance of tiny (few nm) particles on the dissolving calcite surface and their

208   subsequent merging with adjacent particles tends to indicate a heterogeneous growth process that

209   may be initiated as pre-nucleation clusters within the calcite-fluid boundary layer. The growth of

210   the precipitate does not follow a classical homogeneous mechanism[27] that would require the

211   addition of growth building ionic species to step edges and kink sites. Instead, given the

212   limitations of our AFM observations, the first particles already with a diameter of a few

213   nanometers appeared within seconds and at most within 1.5 minutes during one scan on the

214   dissolving calcite surface. To do this, it could be assumed that some ionic species association had

215   already occurred within the fluid boundary layer. Gebauer et al.[28] have shown that stable pre-

216   nucleation ion clusters of calcium carbonate form even in undersaturated solutions. In our case

217   the Sb-bearing solution is undersaturated with respect to any possible Ca-phase but precipitation

218   is clearly observed on a dissolving surface. The current understanding of the mechanism of phase

219   separation allowing for the initial formation of solid particles is an active topic of research[28]

220   because of the application to many geochemical systems including biomineralisation. However,

221   the formation of stable pre-nucleation clusters can be explained in terms of equilibrium

222   thermodynamics that would promote some form of structural orientation between ions in solution

223   resulting in an association of ionic species forming the initial denser cluster form. From our

224   AFM observations it is not clear whether the initial 1-2 nanometer particles nucleate directly on

225   the calcite surface or arrive at the surface already as "clusters" that have formed as pre-

226   nucleation clusters within the near-surface boundary fluid layer. The latter scenario seems highly

227   likely, given that the observations showed immediate precipitation of particles as soon as the

228   calcite surface was in contact with a Sb-bearing solution.

229   The precipitation of the new phase was observed to increase with a decrease in pH, which is

230   consistent with a faster dissolution rate of calcite at lower pH and therefore a faster release of

231   Ca^{2+} ions required for the precipitation of the new phase. Therefore we could reasonably expect

232   that a Ca-antimonate phase is likely to precipitate at the calcite surface. Initially, these

233   precipitates have a disc shape and do not show facets. With time, they develop facets (Figures

234   S2d and 4). $Ca_2Sb_2O_7$ has an orthorhombic crystal structure similar to weberite (Na_2MgAlF_7)[29],

235   and often forms with a dipyramidal habit unlike oxycalcioroméite, which is isometric. Therefore,

236   the formation of dipyramids in combination with the dominant Raman band at 624 cm^{-1} indicates

237   that the precipitated phase is dominantly orthorhombic $Ca_2Sb_2O_7$. However, additional bands at

238   500 cm^{-1} in the Raman spectrum indicate some of the isometric phase is also present in the

239   precipitates. The structure of the Ca-antimonate has been shown to be sensitive to the presence of

240   ions such as F^-, where increase in these ions within the crystal structure encourages the formation

241   of the isometric rather than the orthorhombic form[30]. Whether the mixed phase is due to a phase

242   transformation during or after the experiment is unclear from the ex-situ data. As Sb-rich fluid is

243   injected in the AFM flow-through cell, the release of Ca ions at the calcite surface, will be more

244   concentrated near active dissolution sites such as at the bottom of etch pits or kinks. Here

245   precipitates are initially more numerous (Figures 1, 2b). At these locations, the concentration

246   products of $Ca_2Sb_2O_7$, and probably oxycalcioroméite, are large enough to reach supersaturation

247   with respect to these minerals and result in their subsequent precipitation. The precipitates grow

248   initially as disc-shaped particles; that agglomerate into larger particles, evolving towards fully

249   crystallized $Ca_2Sb_2O_7$ and oxycalcioroméite crystals. Such a coupled dissolution-precipitation

250   process on carbonates has also been reported for the precipitation of a Ca arsenate phase on

251   calcite[23] and the formation of a Ca-selenate phase on calcite[22]. These examples provide a

252   mechanism of possible sequestration of environmentally harmful elements. More generally, such

253   coupled replacement reactions are widespread in mineral-water systems[31] whenever the release

254   of ions from the dissolving mineral is coupled to the precipitation of a new phase at the surface

255   of a dissolving mineral.

256   *Environmental implications*: The present results show that coupled to calcite dissolution, Ca -

257   Sb phases precipitate as nanometer size particles on the calcite surface (heterogeneous

258   nucleation). Primary nanoparticles are then self-assembled into rounded aggregates that coalesce

259   to form larger particle aggregates averaging 130-220 nm wide and up to 80 nm high that cover

260   the carbonate surface. There are much fewer particles at high (8) than low (2.5) pH and fewer

261   particles in the presence of Sb(III) than in the presence of Sb(V). As confirmed by Raman

262   spectroscopy, these particles are predominately $Ca_2Sb_2O_7$ (and probably minor

263   oxycalcioroméite). Furthermore, we could not find any evidence for the formation of the

264   hydrated romeite crystalline salt $Ca[Sb(OH)_6]_2$, that has been suggested to explain unexpectedly

265   low Sb concentrations in extracts of alkaline soils[1,12,32]. This phase may possibly form at higher

266   pH values that could be consistent with ground water in alkaline soils. If this phase was present

267   in the experiments, it could not be detected in the Raman data.

268   As a consequence of the interaction of calcite surfaces with Sb-bearing solutions, antimonate

269   can be sequestered in a solid form on calcite surfaces by a coupled dissolution-precipitation

270   process in a boundary fluid layer. These results provide a mechanistic understanding of

271   environmental studies where a Ca-antimonate phase was proposed to form, but could not

272   previously be observed in-situ[1,4,12]. Therefore, it is reasonable to suggest that calcite or other

273   soluble Ca-bearing surfaces could provide a realistic environmental remediation strategy in the

274   case of elevated Sb concentrations related to acid mine drainage systems, contaminated shooting

275   range soil and ashes from waste incineration.
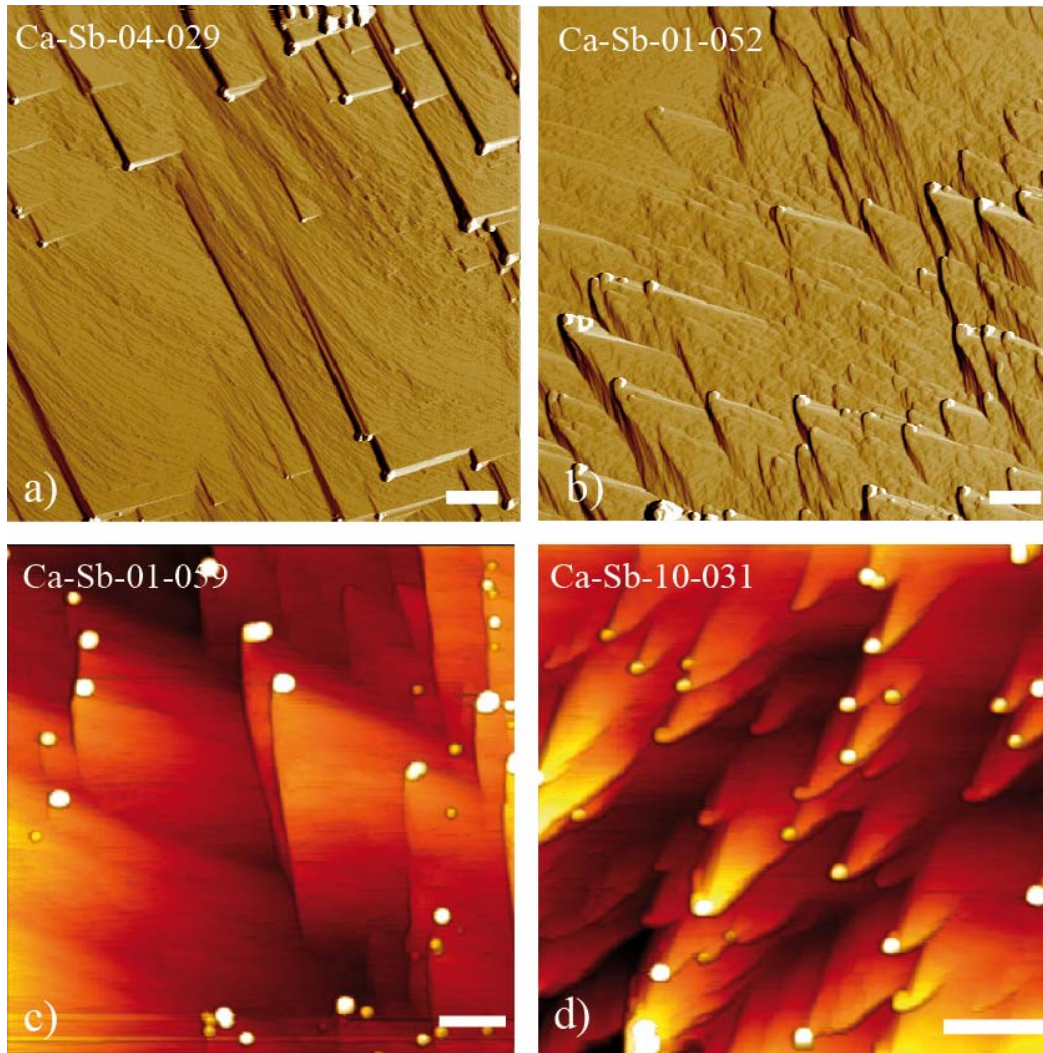
Figure 1. AFM images showing nucleation of precipitates (white spots) at step kinks on a calcite surface. a-c) 2D images in deflection mode. c-d) 3D rendering in height mode. Solution compositions are: a) 50 ppm Sb(V), pH 3.2. b-c) 200 ppm Sb(V), pH 3; d) 5 ppm Sb(III), pH 3 (here probably the Sb(III) oxidized into Sb(V)). These data demonstrate that the antimony-rich precipitates nucleate near step kinks where supersaturation with respect to the new phase is also most likely. Deposits pin the steps at those points and thus inhibit dissolution locally as the steps dissolve around them, hence the appearance of the finger-like morphology emanating from these pinned points. Scale bar 1 µm.
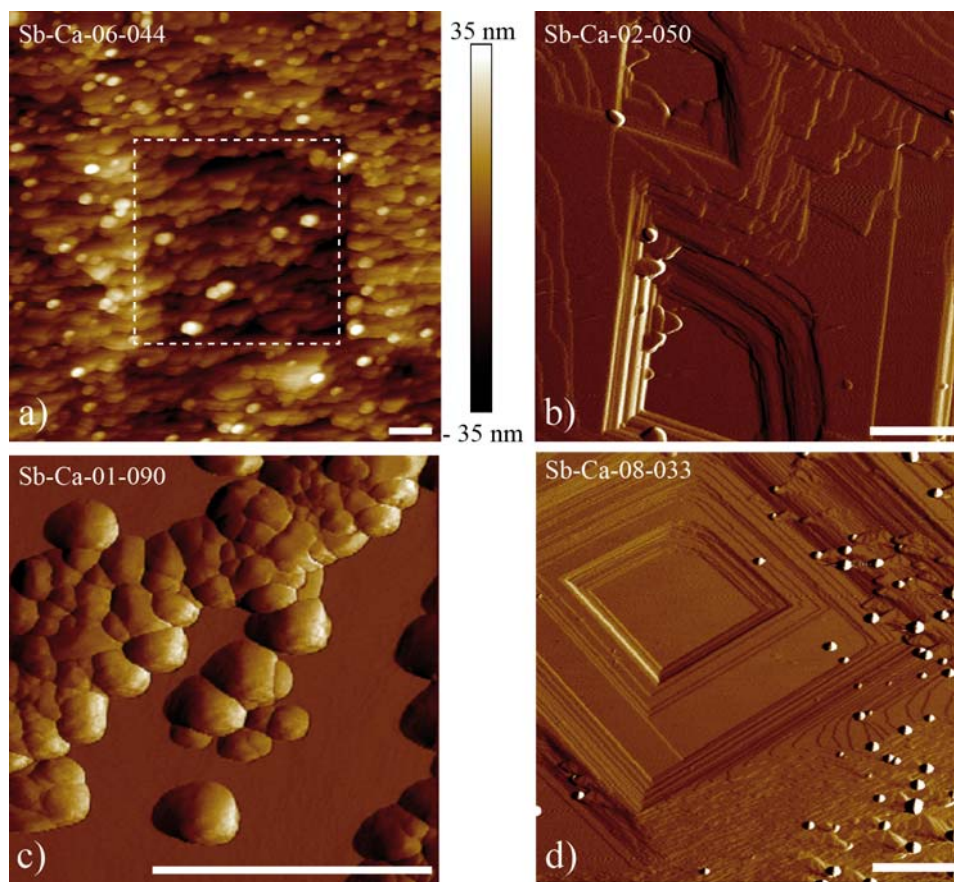
Figure 2. AFM images (deflection mode) of calcium-antimony precipitates on a calcite surface.

Scale bar: 1 μm for all images. a) Calcite surface, 10x10 μm^2, covered with calcium-antimonate

precipitates. The central area, outlined by a dashed square, corresponds to a 5x5 μm^2 area

scanned previously and contains less precipitates. This demonstrates that precipitates are weakly

attached as some are removed by the AFM tip during scanning. Solution Sb(V) 200 ppm, pH 2.5.

b) Etch pits on calcite surface with precipitates along actively dissolving edges. The location of

the precipitates is related to the location of higher dissolution. Solution Sb(V) 200 ppm, pH 5.1.

c) Image (deflection mode) of a calcite surface after 12 hours in solution Sb(V) 200 ppm, pH 3

showing precipitates of calcium-antimonate that form individual patches that then agglomerate.

d) Image (deflection mode) of a calcite surface in solution Sb(III) 10 ppm pH 3, with very few

precipitates of calcium-antimonate demonstrating that Sb(III) form much fewer precipitates.

297
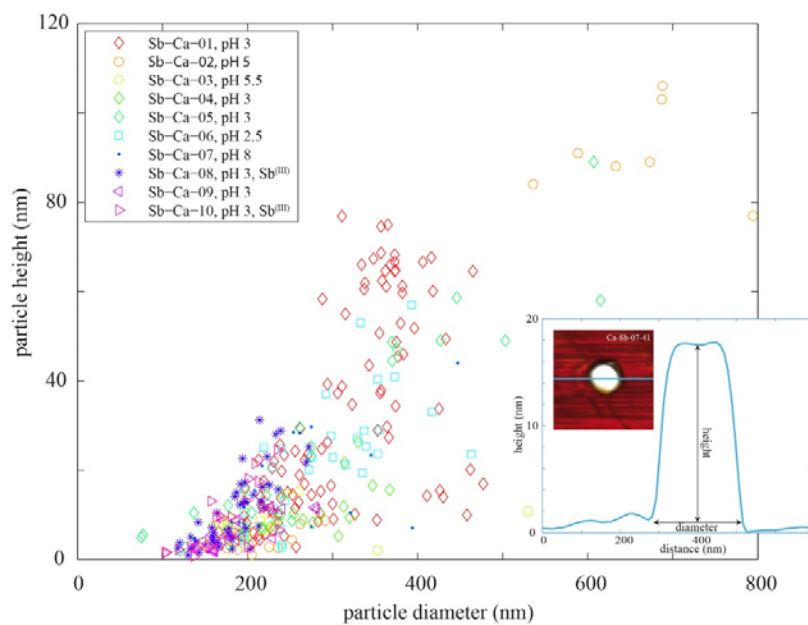
Figure 3. Height versus diameter of Ca-Sb nanoparticles in all AFM experiments. Inset: Height

profile across a nanoparticle and definition of the height and diameter.

300
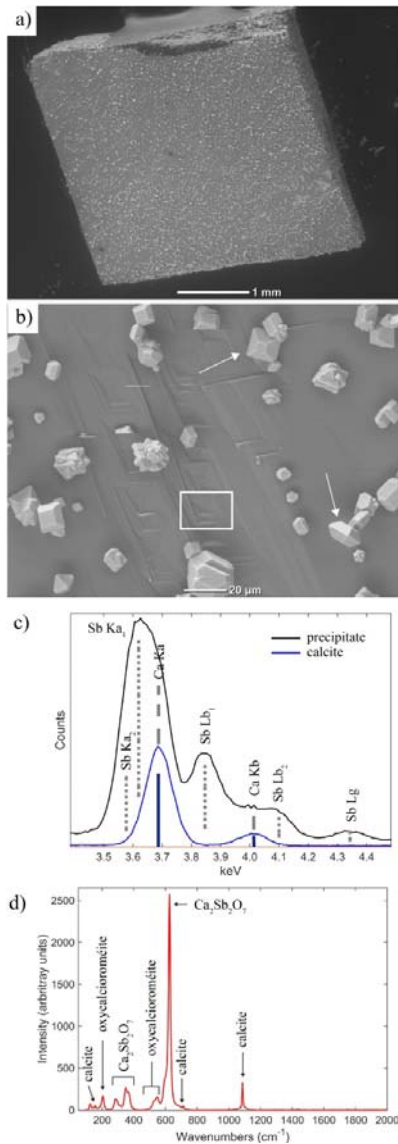
Figure 4. SEM images and EDX and Raman spectra of Ca-Sb precipitates. a) SEM image of the

calcite surface with precipitates at the surface (exp. Sb-Ca-5). b) Higher resolution image of the

precipitates showing their typical dipyramidal structures (white arrows) and the presence of etch

pits on the underlying calcite surface (white box). c) EDX spectra focused on the region between

3.4 and 4.5 eV showing the overlapping Sb, Ca peaks (blue: underlying calcite surface, grey:

precipitate). d) Typical Raman spectrum of the precipitate with phases labelled based on

published spectra for oxycalcioroméite[20] and $Ca_2Sb_2O_7$ (Ref. 17).

308

ASSOCIATED CONTENT

Supporting Information. The supplementary Information file (pdf file) contains: Text

(Experimental conditions), Figure S1; Figure S2; Figure S3; Table S1; and Table S2.

AUTHOR INFORMATION

Corresponding Author

*François Renard, Department of Geosciences, PGP, University of Oslo, box 1048, 0316

Blindern, Oslo, Norway (francois.renard@geo.uio.no)

Author Contributions

CVP and FR performed the experiments and wrote the manuscript. HK acquired and interpreted

the Raman and SEM data. GMH, GB and GO participated to the interpretations of the

experimental data and their consequences for the environment. All authors have given approval

to the final version of the manuscript.

325

REFERENCES

327   (1) Okkenhaug, G.; Zhu, Y. G.; Luo, L.; Lei, M.; Li, X.; Mulder, J. Distribution, speciation and

328   availability of antimony (Sb) in soils and terrestrial plants from an active Sb mining area.

329   *Environmental Pollution* **2011**, *159(10)*, 2427-2434.

330   (2) Stromseng, A. E.; Ljones, M.; Bakka, L.; Mariussen, E. Episodic discharge of lead, copper

331   and antimony from a Norwegian small arm shooting range. *Journal of Environmental*

332   *Monitoring* **2009**, *11(6)*, 1259-1267.

333   (3) Okkenhaug, G.; Almås, Å. R.; Morin, N., Hale; S. E., Arp, H. P. H. The presence and

334   leachability of antimony in different wastes and waste handling facilities in Norway.

335   *Environmental Science: Processes Impacts* **2015**, *17(11)*, 1880-1891.

336   (4) Scheinost, A. C.; Rossberg, A.; Vantelon, D.; Xifra, I.; Kretzschmar, R.; Leuz, A. K.;

337   Funke, H. Johnson; C. A. Quantitative antimony speciation in shooting-range soils by EXAFS

338   spectroscopy. *Geochimica et Cosmochimica Acta* **2006**, *70(13)*, 3299-3312.

339   (5) Okkenhaug, G.; Gebhardt, K. A. G.; Amstaetter, K.; Bue, H. L.; Herzel, H.; Mariussen, E.;

340   Almås, A. R.; Cornelissen, G.; Breedveld, G. D.; Rasmussen, G.; Mulder, J. Antimony (Sb) and

341   lead (Pb) in contaminated shooting range soils: Sb and Pb mobility and immobilization by iron

342   based sorbents, a field study. *Journal of Hazardous Materials* **2016**, *307*, 336-343.

343   (6) Filella, M.; Belzile, N.; Chen, Y. W. Antimony in the environment: a review focused on

344   natural waters: I. Occurrence. *Earth-Science Reviews* **2002a** *57(1)*, 125-176.

345   (7) Leyva, A. G.; Marrero, J.; Smichowski, P.; Cicerone, D. Sorption of antimony onto

346   hydroxyapatite. *Environmental Science & Technology* **2001**, *35(18)*, 3669-3675.

347   (8) Filella, M.; Belzile, N.; Chen, Y. W. Antimony in the environment: a review focused on

348   natural waters: II. Relevant solution chemistry. *Earth-Science Reviews* **2002b**, *59(1)*, 265-285.

349   (9) Nicolli, H. B.; Suriano, J. M.; Gomez Peral, M. A.; Ferpozzi, L. H.; Baleani, O. A.

350   Groundwater contamination with arsenic and other trace elements in an area of the Pampa,

351   Province of Córdoba, Argentina. *Environmental Geology* **1989**, *14(1)*, 3-16.

352   (10) Liu, F.; Le, X. C.; McKnight-Whitford, A.; Xia, Y.; Wu, F.; Elswick, E.; Johnson, C.;

353   Zhu, C. Antimony speciation and contamination of waters in the Xikuangshan antimony mining

354   and smelting area, China. *Environmental Geochemistry and Health* **2010**, *32(5)*, 401-413.

355   (11) Brugger, J.; Gieré, R.; Graeser, S.; Meisser, N. The crystal chemistry of roméite.

356   *Contributions to Mineralogy and Petrology* **1997**, *127(1-2)*, 136-146.

357   (12) Johnson, C. A.; Moench, H.; Wersin, P.; Kugler, P.; Wenger, C. Solubility of antimony

358   and other elements in samples taken from shooting ranges. *Journal of Environmental Quality*

359   **2005** *34(1)*, 248-254.

360   (13) Cornelis, G.; Van Gerven, T.; Snellings, R.; Verbinnen, B.; Elsen, J.; Vandecasteele, C.

361   Stability of pyrochlores in alkaline matrices: Solubility of calcium antimonate. *Applied*

362   *Geochemistry* **2011**, *26*, 809-817.

363   (14) Cornelis, G.; Johnson, C. A.; Van Gerven, T.; Vandecasteele, C. Leaching mechanisms of

364   oxyanionic metalloid and metal species in alkaline solid wastes: a review. *Applied Geochemistry*

365   **2008**, *23(5)*, 955-976.

366   (15) Ruiz-Agudo, E.; Putnis, C. V. Direct observations of mineral-fluid reactions using atomic

367   force microscopy: the specific example of calcite. *Mineralogical Magazine* **2012**, *76*, 227–253.

368   (16) Edwards, H.G.M.; Villar, S.E.J.; Jehlicka, J.; Munshi T. FT-Raman spectroscopic study of

369   calcium-rich and magnesium-rich carbonate minerals. *Spectrochimica Acta Part A* **2005**, *61*,

370   2273-2280.

371   (17) Gedzeciviute, V.; Welter, N.; Schüssler, U.; Weiss, C. Chemical composition and

372   colouring agents of Roman mosaic and millefiori glass, studied by electron microprobe analysis

373   and Raman microspectroscopy. *Archaeological and Anthropological Sciences* **2009**, *1*, 15-29.

374   (18) Itukara, T.; Sasai, R.; Itoh, H. Detoxification of antimonic contaminated water and

375   precipitation recovery of antimony by mineralization under hydrothermal condition. *Chemical*

376   *Letters* **2007**, *36*, 524-525.

377   (19) King, H. E.; Mattner, D. C.; Plümper, O.; Geisler, T.; Putnis, A. Forming cohesive

378   calcium oxalate layers on marble surfaces for stone conservation. *Crystal Growth Design* **2014**,

379   *14*, 3910-3917.

380   (20) Biagioni, C.; Orlandi, P.; Nestola, F.; Bianchin, S. Oxycalcioromeite, $Ca_2Sb_2O_6O$, from

381   Buca della Vena mine, Apuan Alps, Tuscany, Italy: a new member of the pyrochlore supergroup.

382   *Mineralogical Magazine* **2013**, *77*, 3027-3038.

383   (21) Renard, F.; Montes-Hernandez, G.; Ruiz-Agudo, E.; Putnis, C. V. Selenium incorporation

384   into calcite and its effect on crystal growth: An atomic force microscopy study. *Chemical*

385   *Geology* **2013**, *340*, 151-161.

386 (22) Putnis, C. V.; Renard, F.; King, H.; Montes-Hernandez, G.; Ruiz-Agudo, E. Sequestration

387 of selenium on calcite surfaces revealed by nanoscale imaging. *Environmental Science &*

388 *Technology* **2013**, *47*, 13469–13476.

389 (23) Renard, F.; Putnis, C. V.; Montes-Hernandez, G.; Ruiz-Agudo, E.; Hovelmann, J.; Sarret,

390 G. Interactions of arsenic with calcite surfaces revealed by in-situ nanoscale imaging.

391 *Geochimica et Cosmochimica Acta* **2015**, *159*, 61–79.

392 (24) Ruiz-Agudo, E.; King, H. E.; Patiño-López, L. D.; Putnis, C. V.; Geisler, T.; Rodriguez-

393 Navarro, C.; Putnis, A. Control of silicate weathering by interface-coupled dissolution-

394 precipitation processes at the mineral-solution interface. *Geology* **2016**, *44(7)*, 567-570.

395 (25) Putnis, A.; Putnis, C. V. The mechanism of reequilibration of solids in the presence of a

396 fluid phase. *Journal of Solid State Chemistry* **2007**, *180(5)*, 1783-1786.

397 (26) Putnis, A. Mineral replacement reactions. *Reviews in Mineralogy and Geochemistry* **2009**,

398 *70(1)*, 87-124.

399 (27) Teng, H.H. How ions and molecules organize to form crystals. The mineral-water

400 interface. *Elements* **2013**, *9*, 189-194.

401 (28) Gebauer, D.; Kellermeier, M.; Gale, J.D.; Bergström, L.; Cölfen H. Pre-nucleation clusters

402 as solute precursors in crystallization. *Chemical Society Reviews* **2014**, *43*, 2348-2371.

403 (29) Chelazzi, L.; Borrini, D.; Bonazzi, P. $Ca_2Sb_2O_7$–$Ca_3Mn^{2+}Sb_4^{5+}O_{14}$ pseudo-binary system:

404 Synthesis and characterization by X-ray powder diffraction. *Solid State Sciences* **2011**, *13*, 195-

405 197.

406   (30) Aia, M. A.; Mooney, R. W.; Hoffman, C. W. W. An X-Ray Study of pyrochlore

407   Fluoantimonates of calcium, cadmium, and manganese. *Journal of The Electrochemical Society*

408   **1963**, *110*, 1048-1054.

409   (31) Putnis, A. Mineral replacement reactions: from macroscopic observations to microscopic

410   mechanisms. *Mineralogical Magazine* **2002**, *66(5)*, 689-708.

411   (32) Oorts, K.; Smolders, E.; Degryse, F.; Buekers, J.; Gascó, G.; Cornelis, G.; Mertens, J.

412   Solubility and toxicity of antimony trioxide (Sb_2O_3) in soil. *Environ. Sci. Technol*. **2008**, 42,

413   4378.